Applying fluorescence in situ hybridization to aquatic systems with cyanobacteria blooms: Autofluorescence suppression and high-throughput image analysis

Ashley B. Cohen [ORCID],* Asher Novkov-Bloom, Christian Wesselborg, Milana Yagudaeva, Elizabeth Aranguiz, Gordon T. Taylor [ORCID]
School of Marine and Atmospheric Sciences, Stony Brook University, Stony Brook, New York

Abstract

Cyanobacterial Harmful Algal Blooms (CyanoHABs) are expanding geographically in both fresh and marine water bodies due to coastal eutrophication and global climate change and are restructuring the microbial ecology of these systems. Cyanobacterial autofluorescence can pose a significant impediment to accurately identifying prokaryotic taxonomic groups in environmental samples using fluorescence in situ hybridization (FISH). This can hinder our ability to accurately quantify, and therefore fully understand ecological changes. As abundances of FISH target cells and autofluorescent cells can often be of the same the order of magnitude, simply subtracting average autofluorescent cell concentrations—determined from enumerating unhybridized samples— yields apparent concentrations of target cells with unacceptably large analytical uncertainty. Here we present a $CuSO_4$/EtOH chemical pretreatment protocol that significantly reduces undesirable autofluorescence in hybridized environmental samples. We apply a novel data filtration routine to FISH images that efficiently removes residual autofluorescent cells from final cell counts. We then subject images to an automated image analysis routine that accurately enumerates probe-positive cells. This method is inexpensive and easy to implement as part of a routine FISH workflow. By applying this method to cyanobacteria rich samples, we can better understand how microbial community changes are contributing to globally changing biogeochemical cycles.

Cyanobacteria harmful algal blooms (CyanoHABs) are becoming more geographically extensive in fresh and marine water bodies as a consequence of coastal eutrophication and global climate change and appear to be restructuring the microbial ecology of these systems (Hallegraeff 2010; O'Neil et al. 2012; Wells et al. 2015). Lower trophic level organisms, such as prokaryotes and protists, tolerate much lower concentrations of cyano-toxins than those at higher trophic levels. CyanoHABS therefore weaken the efficiency of the microbial loop in the biological carbon pump, which results in greater organic matter deposition in sediment. In turn, the higher sedimentary organic matter content causes hypoxic or anoxic conditions lethal to benthic macrofauna living near the sediment–water interface. Additionally, if the affected microbes are key to the food web, their decimation causes trophic cascades (Christoffersen 1996). One major focus of current research on bloom-forming harmful cyanobacteria is quantifying how cyanobacteria interact with other microbes and affect the overall microbial ecology (e.g., Parulekar et al. 2017; Tromas et al. 2017). Tromas et al. (2017) even used such information to develop a predictive cyanobacteria bloom model. As such, accurately quantifying population dynamics within microbial communities over time is critical. Relative and absolute abundances of taxa derived from rRNA libraries often used in such studies are poorly constrained proxies for cell abundances because of potential PCR biases and because prokaryotes can have anywhere between 1 and 15 copies of the 16S rRNA gene per cell (Kembel et al. 2012). This uncertainty seems to be even more pronounced for 18S rRNA libraries representing microbial eukaryotes. For example, Gong and Marchetti (2019) demonstrated that among a handful of eukaryotic microalgae, 18S gene copies can vary from 3 to 160 per cell as evident from draft/closed genomes. In the common situation that environmental or experimental samples have to be split for many analyses, sample volumes can also often be too small to extract sufficient DNA for metagenomic sequencing or quantitative PCR.

The small volume requirements, application versatility (e.g., high throughput counting by flow cytometry), and its ability to associate phylum-to-genus level taxonomic information with individual cells make fluorescence in situ hybridization (FISH) an ideal tool for CyanoHAB field surveys and for incubation experiments that quantitatively track changes in microbial community composition and activity over time (e.g., stable isotope probing, feeding experiments) (Jezbera et al. 2005; Huang et al. 2009). The FISH method irreversibly binds a fluorophore-conjugated oligonucleotide sequence (typically 16 to 25-mer), unique to a taxonomic group of interest, to rRNA molecules in target cells. These cells then "light up" when viewed under a fluorescence microscope or sensed by a flow cytometer.

Environmental samples usually contain both eukaryotic and prokaryotic autofluorescent photoautotrophic cells. However, microalgae typically do not impede FISH studies of prokaryotes, primarily because of their larger size and distinctive cell morphologies. In contrast, autofluorescence from cyanobacteria, green sulfur bacteria and purple sulfur bacteria can pose severe methodological problems for recognition of FISH targets and enumeration of similarly shaped and sized prokaryotic cells in many aquatic systems. When autofluorescent cells are mistaken for probe-positive targets in an autofluorescence-plagued census, cell abundances of target taxa are overestimated which can result in misleading conclusions about relationships between particular taxa and experimental variables.

Cyanobacterial autofluorescence originates primarily from the pigments Chlorophyll *a* (Chl *a*), (allo)phycocyanin and phycoerythrin. Phycoerythrin autofluorescence is evident through Cy3 and FITC fluorescence microscopy filter sets and (Allo)phycocyanin autofluorescence is visible through the Cy5 filter set (Lamb et al. 2018) (Tables SI and 1). Chl *a* fluoresces through the FITC filter set, but is not visible through the Cy3 or Cy5 filter sets because of mismatches between excitation and emission wavelength ranges (Tables S1 and 1). Therefore,

Chl *a* autofluorescence can be avoided by using the appropriate filter set.

Green sulfur bacteria contain bacteriochlorophylls *a*, *c*, *d*, and *e* in light harvesting complexes in structures called chlorosomes (Olson 2013). Chlorosome pigments are in a highly aggregated state, with bacteriochlorophyll *a* being in a small protein envelope. Compared to measurements in polar solvents, in vivo and fixed cell fluorescence is significantly red-shifted, with the fluorescence excitation and emission maxima wavelengths for the entire chlorosome being 460 and 740 nm and 750 and 801 nm (Olson 2013). These wavelengths do not overlap significantly with any of the excitation and emission wavelength ranges for the Cy3, Cy5, or FITC filter sets and therefore do not impede routine FISH analyses.

All purple sulfur bacteria cells contain bacteriochlorophyll *a* and the carotenoid okenone. Only six known purple sulfur bacteria possess bacteriochlorophyll *b*. The fluorescence excitation and emission wavelength ranges of okenone overlap with those of the Cy3, but not the Cy5 filter set. When measured in vivo or in fixed cells, bacteriochlorophylls *a* and *b* do have a small excitation peak between 550 and 600 nm (overlapping with Cy3 excitation), but the emission wavelengths are in the far-red, between 850 and 985 nm (Oelze 1985; Permentier et al. 2001). We found that purple sulfur bacteria are not problematic in practice because they completely lose their purple color viewed under brightfield after the final ethanol rinse step of the FISH protocol detailed in Pernthaler et al. (2001). Like chlorophylls and other carotenoids, okenone is ethanol-soluble and is extracted from the cells. Unfortunately, the ethanol rinse step does not remove phycoerythrin and phycocyanin from cyanobacteria because they are not ethanol soluble. Thus, autofluorescence by cyanobacteria, in particular, persists after FISH preparation and its suppression is therefore the focus of this study.

Chemical treatments have been developed to suppress autofluorescence from cyanobacteria and microalgae cells in pure cultures and natural water samples after FISH and prior

Table 1. Spectral characteristics of common autofluorescent pigments and spectrally overlapping FISH fluorophores. FWHM = full width at half maximum peak height, a standard measure of the bandwidth transmitting at least 50% of the radiation. Chl *a* has two excitation/emission maxima, which are presented in the format e1/e2.

Pigment	Excitation max. (nm)	Excitation FWHM (nm)	Emission max. (nm)	Emission FWHM (nm)	Overlapping dye
(Allo) Phycocyanin[*]	(650) 620	(575-675) 550–650	(660) 644	625–675	Cy5
Phycoerythrin[†]	565	475–575	576	560–595	Cy3; FITC
Okenone[‡]	490	480–560	596	580–630	Cy3
Chl *a*[§]	417/665	400–490/650–675	685/722	675–720/699–744	FITC

[*]Sobiechowska-Sasim et al. (2014), Lamb et al. (2018).
[†]Sobiechowska-Sasim et al. (2014).
[‡]Codgell et al. (1990), Toropygina et al. (2005), Polli et al. (2006).
[§]Dixon et al. (2005); Du et al. (1998); Frankenberg and Berry (2018).

to Raman microspectroscopy. For example, Zeller et al. (2016) treated samples with varying concentrations of $CuSO_4$ and H_2O_2 to decrease cyanobacterial autofluorescence visible through the Cy3 and FITC microscope filter sets after FISH, directly before mounting filters on slides. While the treatments did decrease the number of false positive cells, autofluorescent cells were not entirely eliminated. Thus, the method still requires the enumeration and subtraction of autofluorescent cell blanks. This is time consuming and results in undesirable error propagation.

Yakubovskaya et al. (2019) developed a chemiphotobleaching technique, by which the activity of 3% H_2O_2 was enhanced by illuminating with a standard diode lamp and completely suppressed autofluorescence in cyanobacterial and microalgal cultures. This treatment did not alter cellular Raman spectra, indicating that it is gentle enough for downstream microspectroscopy applications. This technique was successfully applied to diatom-rich natural samples (Yakubovskaya et al. 2019), but has yet to be applied to cyanobacteria-rich natural samples.

Autofluorescence suppression treatments in combination with Cy5-FISH have not yet been explored in environmental studies, although this fluorophore is typically used to hybridize autofluorescent samples in medical analyses (Ibey et al. 2003). Furthermore, there is no established method, beyond crude subtraction of average autofluorescent cell counts, for filtering out residual autofluorescence signals after chemical treatment. In this paper, we present methods to suppress cyanobacterial autofluorescence in environmental samples prior to Cy5-FISH and for accurately enumerating probe-positive targets in the resulting fluorescent micrographs using image analysis. In addition to population censuses, this method can in theory be used on cyanobacteria-rich samples for paired FISH-microspectroscopy techniques, such as SIP-Raman-FISH.

The method was developed with field samples taken from Fayetteville Green Lake (FGL), NY in July 2018 (Fig. 1a). FGL is an oligotrophic, meromictic, euxinic lake that is famous for its summer "whiting event"—a *Synechococcus gracile* (strain PCC-6307, Genome Taxonomy Database taxonomy *Cyanobium PCC-6307*) bloom that is rapid and sufficiently productive to cause mass precipitation of calcium carbonate (Culver and Brunskill 1969). During the whiting event, *S. gracile* is highly abundant in the oxic zone and near the lower oxycline boundary (defined by the first appearance of dissolved sulfide), attaining cell abundances of as high as $1.5 \times 10^7 \, L^{-1}$ (Schultze-Lam et al. 1997) over the 4–12 m depth range and as much as $2.5 \times 10^9 \, L^{-1}$ over the 19–20.5 m depth range, coinciding with positive dissolved O_2 and pH excursions (Fig. 1b). FGL also has a well-defined bacterial "plate" of highly concentrated biomass consistently observed between 20 and 21 m consisting predominantly of purple and green sulfur bacteria (Havig et al. 2015, 2018). The high concentration of biomass in the bacterial plate is responsible for the sharp peak in

turbidity measurements over this depth range (Fig. 1b). Green sulfur bacterial populations are also routinely observed below the plate as deep as 23 m (Havig et al. 2015, 2018).

Using a FISH probe targeting epsilonbacteraeota, a lower abundance taxon in FGL, we establish that probe target concentrations calculated by subtracting average autofluorescent cells from untreated hybridized cells in a sample yields unacceptably large analytical uncertainties. This illustrates the need for a reliable autofluorescence suppression pretreatment, which we then optimize and evaluate its performance through Cy3, FITC and Cy5 filter sets. Using the superior chemical pretreatment, we establish that Cy5 is the best FISH probe fluorophore conjugate for this application. We then establish where autofluorescence suppression treatments should occur within the standard oligo-FISH workflow (Pernthaler et al. 2001). An automated method for high-throughput image processing and accurate cell enumeration is then presented. This development is particularly critical for Cy5-hybridized cell recognition because Cy5 usually fluoresces too dimly to be enumerated by eye and relies on images captured after relatively long camera exposure times. We then present a data filtration method for excluding residual autofluorescent cells from probe-positive cell counts of $CuSO_4$/EtOH-treated, hybridized samples.

Materials and procedures

Sample collection and filter preparation

The lower oxycline down through upper monimolimnion in the deepest part of FGL (43°03′01.9″N, 75°57′58.9″W) was sampled during 28 July–4 August 2018 during the annual *S. gracile* bloom as part of a FISH survey. Sampling efforts were focused between 19 and 23 m, where we established the total prokaryotic cell concentrations and phycoerythrin concentrations were highest during a prior July survey and where we detected the maximal water column turbidity during the 2018 survey (Figs. S1 and S2, Fig. 1b). We chose to optimize our method using samples with the maximal cyanobacteria cell concentrations for two reasons. First, we wanted to ensure that micrographs were populated with enough autofluorescent cells to validate our method statistically (having a high enough n value). Second, we view these samples as a "worst case scenario"—if the method works for samples with high autofluorescent cell concentrations, it will be robust enough to work for most natural samples. The deeper of two distinct cyanobacterial populations occurred within this depth range with peak abundances at 19.75 m, but significant cyanobacterial cell densities were also evident immediately below this maximum. Samples were collected using a peristaltic pump with a planar weight attached to the sampling end, immediately fixed with freshly 0.2 μm filtered, borate-buffered 2% formaldehyde (final conc.) and frozen at $-20°C$ in 50 mL Falcon tubes. Samples remained frozen until processing. First, DAPI preparations of 2–5 mL subsamples were filtered through

(a) (b)
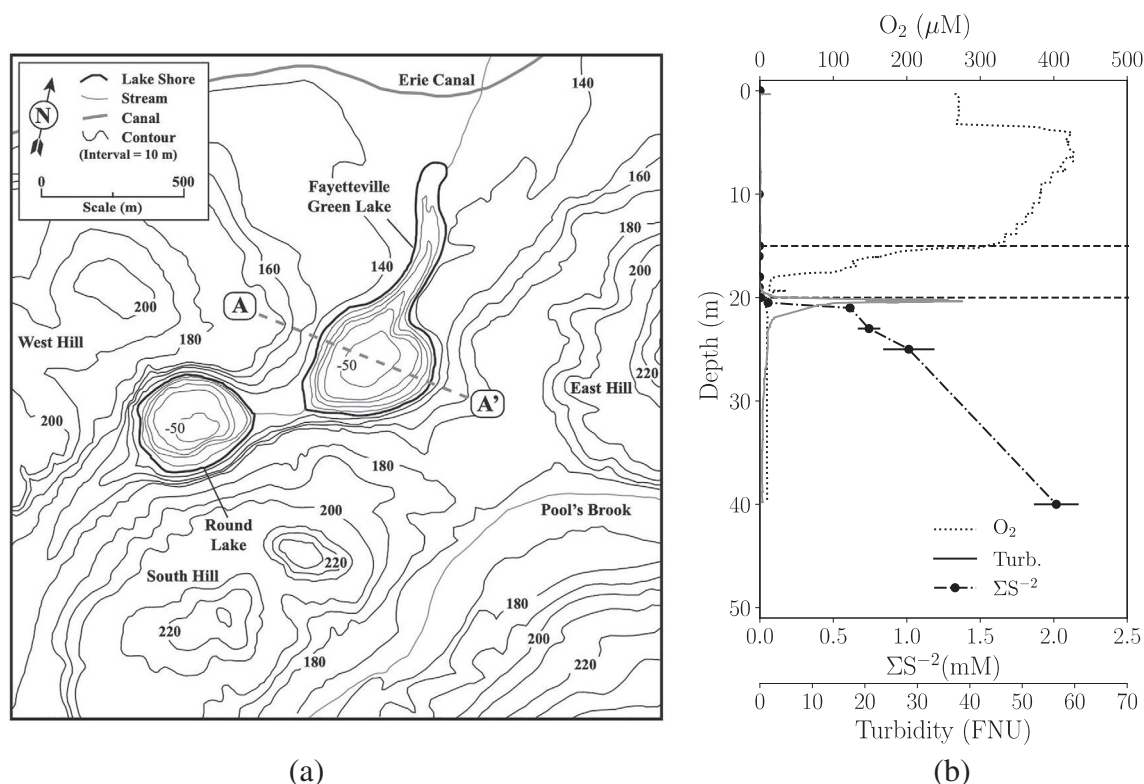
Fig 1. (**a**) Location of Fayetteville Green Lake (FGL) and sampling site (Havig et al. 2018). (**b**) Vertical profile of dissolved oxygen, turbidity, and sulfide at sampling site in FGL measured during the July 2018 *S. gracile* bloom. The dotted horizontal lines indicate the upper and lower boundaries of the oxycline. The dissolved oxygen and turbidity profiles were obtained from continuous measurements provided by a YSI-EXO1 sonde outfitted with an EXO optical dissolved oxygen sensor (measurement range 0–1562.5 μM, accuracy $\pm$ 3.10 μM) and EXO optical turbidity sensor (measurement range 0–4000 FNU, accuracy $\pm$ 0.3 FNU for readings <1000 FNU, otherwise $\pm$ 5% of reading). Sulfide concentrations were determined by measuring discrete samples as in Cline (1969).

25 mm 0.2 μm black polycarbonate membranes to enumerate total microbial cells according to standard protocols (Porter and Feig 1980). To improve cell dispersion, polycarbonate membranes were briefly dipped in freshly 0.2 μ filtered 0.01% Triton X-100 (Sigma-Aldrich) detergent and mounted on water-saturated GF/C backing filters on metal vacuum filtration frits. Because FISH targets can be a small percentage of total cells, FISH subsample volumes were adjusted to achieve cell densities in a microscope field-of-view of about threefold greater than in DAPI preps. FISH subsamples were gently vacuum filtered on to 47 mm 0.2 μm GTTP polycarbonate membranes mounted on sintered glass frits. To serve as a probe-positive FISH control, *Escherichia coli* pure cultures in exponential growth phase were filtered in the same way.

Membranes were air dried in the dark on 3 M™ (3 M Co.) absorbent paper and stored at −20° C in sterile Petri slides. Filters were thawed (∼ 10 min at room temperature) and cut into wedges with EtOH-sterilized scissors such that for each sample, a single filter provided all untreated unhybridized (environmental autofluorescence controls), chemically treated unhybridized (environmental residual autofluorescence controls), chemically treated and hybridized, and chemically untreated hybridized subsamples for a given sample. To enable simultaneous processing of many wedges in one solution during autofluorescence suppression treatment and oligo-FISH, each wedge was labeled with a pencil.

Autofluorescence suppression treatments

Unhybridized samples taken from the depth of maximum autofluorescence (20.5 m) were subjected to a chemiphotobleaching pretreatment (Yakubovskaya et al. 2019) and a strictly chemical pretreatment detailed in Zeller et al. (2016). The chemiphotobleaching protocol was followed exactly as described in Yakubovskaya et al. (2019) with prescribed durations of 2, 4, 6, 10, and 24 h. We focused on Zeller et al.'s (2016) CuSO$_4$/EtOH pretreatments because they outperformed H$_2$O$_2$ at removing autofluorescence in their original experiments. Moreover, the high concentrations of H$_2$O$_2$ required for the Zeller et al. (2016) treatment would likely be destructive to prokaryotic cells, making them unsuitable for FISH methods.

Working stock solutions (100X) of CuSO$_4$ were made from ACS reagent-grade CuSO$_4$*5H$_2$O and stored at room temperature in total darkness. CuSO$_4$ solutions of several concentrations (1.29, 2.0, and 4.0 mM) were freshly prepared from their 100X stocks, diluted with Milli-Q water and filter sterilized

through a sterile 0.2 μm polyethersulfonate Whatman® Puradisc™ syringe filter directly into a sterile Petri dish before use. Molecular reagent-grade absolute ethanol (EtOH) was decanted into a separate sterile Petri dish right before use. Two sets of labeled unhybridized filter wedges per $CuSO_4$ concentration were sequentially immersed in the $CuSO_4$ solution and then in EtOH, followed by drying on 3M™ absorbent paper (3 M Co.). Each step had a 10 min duration and was performed at room temperature in the dark. For each $CuSO_4$ concentration tested, one set of wedges was counterstained with DAPI (detailed in Pernthaler et al. 2001) before $CuSO_4$/EtOH treatment and one set of wedges was DAPI counterstained after $CuSO_4$/EtOH treatment and drying.

Slide preparation and microscopy

Filter wedges of chemically-treated and untreated samples were mounted on glass slides with a 4 : 1 mixture of Citifluor™ (Ted Pella, Inc.) and Vectashield® (Vector Laboratories Inc.) mounting solutions under a cover slip and examined by epifluorescence microscopy. The chemically-treated unhybridized samples served to determine how much residual cellular autofluorescence (if any) remained after the treatment relative to the untreated, unhybridized control samples. To optimize camera exposure times, monochrome micrographs were taken in randomly selected fields-of-view using a Zeiss Axioscope epifluorescence microscope coupled to an Optronics MagnaFire™ CCD camera. Cy3, Cy5, FITC, and DAPI images were taken at 630X or 1000X magnification in the same fields-of-view. Magnification of all micrographs for a given sample was kept constant, because observed target brightness varies with objective lenses.

For each filter set, camera exposure times were kept constant to allow direct quantitative comparisons. For Cy3, Cy5, FITC, and DAPI, the exposure times were 3.2 s, 2 min, 2.1 s, and 3.2 s, respectively. Cy3 and Cy5 monochrome images were taken in the camera's red channel, FITC images were taken in the green channel, and DAPI monochrome images were taken using the camera's infrared cut channel. Individual channels were chosen based on the emission spectra of the dyes (Table S1). To confirm that chosen channels did not omit any stained cells, micrographs produced in each channel were compared to the IR cut channel. We found that for Cy3 and Cy5, all information was contained in the red channel, while for FITC all information was contained in the green channel. This single channel approach was necessary due to the prohibitively long exposure times ($\geq$ 10 min) required for the camera to mechanically cycle through multiple filters to produce a broad spectrum (IR cut) image from dimly fluorescing Cy5-labeled specimens.

Oligo-FISH

After establishing the optimal $CuSO_4$ concentration, both $CuSO_4$/EtOH-treated and untreated filter wedges with environmental samples or *E. coli* cells were subjected to a standard oligo-FISH protocol (Pernthaler et al. 2001). Environmental sample wedges were hybridized against the Cy5-Eps682 probe (CGG ATT TTA CCC CTA CAC) (Lin et al. 2006), while *E. coli* wedges were hybridized against the Cy5-Gam42a (GCC TTC CCA CAT CGT TT) probe with the competitor probe Bet42a (GCC TTC CCA CTT CGT TT) (Manz et al. 1992). 50 μL of a 50 ng μL^{-1} FISH probe working solution and 450 μL of hybridization buffer were added to wells in a sterile 24 well cell culture plate (Corning Incorporated Costar®) and mixed by pipetting up and down. Wedges were carefully immersed in the solution and positioned using a pair of ethanol-sterilized tweezers. A single well can accommodate up to 20 samples wedges. Hybridizations were performed at 46°C for 3 h using a 35% formamide hybridization buffer. All sample wedges were counterstained with 1 μg mL^{-1} DAPI after hybridization as detailed in Pernthaler et al. (2001). Slide preparation and microscopy was performed in the same way as for the unhybridized $CuSO_4$/EtOH-treated and untreated samples, except images were only taken through microscope filter sets appropriate for the probe fluorophore and the DAPI counterstain. For each sample, 15–20 images were captured from randomly selected fields-of-view.

Image analysis of micrographs

Methods described below were performed on all sample types to enumerate cells. The manual method and Methods 2 and 3 were also used to quantify micrograph cell and background fluorescence as pixel gray values.

Manual

Before any automated procedures were tested, cell and background fluorescence of micrographs were quantified manually using the Fiji distribution of ImageJ by the following routine (Schneider et al. 2012). Original micrographs were converted to a 16-bit RGB images and background was subtracted using a rolling ball radius of 20 pixels. The image threshold was then manually adjusted and applied to convert the thresholded image to a binary mask. For this step, the "Otsu," "Bernsen," and "Default" ImageJ thresholding methods were compared. Background speckling was cleaned by using the "Despeckle" function. Prior to any further processing, the image's spatial scale was set to the true microscope scale. The "Analyze Particles" function was then run with a minimum area cut-off equal to the area of the membrane pore size. Particle analysis output was chosen to include area, area integrated intensity, and mean gray-scale value measurements. Cells identified by this routine were added to the Region of Interest (ROI) manager.

The original image was then reopened and once again converted to a 16-bit RGB file, but no background correction was applied. All ROIs combined was selected to measure the area, integrated density, and mean gray-scale value of all cells as one area in the original image or to measure individual cells (keeping ROIs separate, but measuring them all at once)

using the ROI manager "Measure" tool. The first approach is used when all cells in the image are the "same" and counting is not needed (i.e., area-normalized fluorescence measurements of all pretreated unhybridized cells or all hybridized probe-positive cells). When cell counting is required or not all cells are the same (a mixture of hybridized and autofluorescent cells), the area, integrated density, and mean gray-scale value of individual cells were measured by selecting all individual ROIs and measuring them at once, but without first combining all of the ROIs into one merged ROI.

In both cases, the image background was identified by selecting the entire non-cell area. The "Results" data table of measurements from cells and the background were saved and later used to calculate the background-corrected cell fluorescence intensity per cell area, the background fluorescence intensity per background area, and cell counts. The background-corrected cell fluorescence per cell area f_c (fluorescence intensity as gray pixel value/μm^2) is defined by Eq. 1.

$$f_c = \frac{(I_c - A_c \times g_b)}{A_c},\tag{1}$$

where A_c is cell area (μm^2) of a single cell or the combined cell area, I_c is integrated fluorescence density of a single cell or the combined cell area (pixel gray value on a scale of 0–255), and g_b is the mean gray-scale value of the background (corresponding to fluorescence intensity as pixel gray value on a scale of 0–255 per background area (μm^2).

Automated

Because Cy5 fluorescence is very weak and often invisible to the human eye, Cy5-hybridized cells can only be reliably enumerated at an acceptable rate by image analysis of micrographs acquired by long camera exposure times. An automated image analysis procedure that accurately performs cell counting and fluorescence analyses of FISH samples is highly desirable, but also challenging.

Typically, cells are concentrated on a membrane for FISH such that the least abundant target taxa are not below the method's detection limit. That same sample then usually has to be subsampled for hybridizations against multiple probes due to limited sample availability. This often results in micrographs with overcrowded target cells if probing for higher abundance taxa. We therefore desired an automated method that can accurately count cells at low to high cell densities. Several methods of automated cell counting were evaluated and compared to manual cell counts.

Method 1: Python image analysis

The first automated method utilized the Python Sci-kit learn library (Pedregosa et al. 2011). To account for variability in factors such as dimness/exposure and focus, image histograms were first matched to that of an image selected to represent the ideal exposure conditions. An unprocessed sample

Cy5 image acquired at 630X magnification is shown in Fig. 2a and compared to the processed image after histogram matching (Fig. 2b). Dynamic thresholding, as suggested by Riccio et al. (2018), was then applied using the "weighted mean local pixel neighborhood" method (Fig. 2c). Light spots (cells) were defined as collections of pixels with an intensity ≥0.15 on a scale of 0 to 1. A seed mask was created using the defined light spots.

To create the background mask from the thresholded image, edge detection was enhanced using a Sobel filter (Fig. 2d), and then a Gaussian blur with standard deviation, $\sigma = 2$, was applied (Fig. 2e). We then subjected the blurred, edge enhanced image and the seed mask to a watershed transform. This segments the gray-scale image by treating it as a topographic map, with the heights defined by the pixel intensity, and draws dividing lines that follow the "tops of the ridges." Fig. 2f shows the various segments as regions with constant gray value. For images that are mostly light objects on a dark background, such as epifluorescence micrographs, the background can be defined as the segment with the greatest number of pixels (i.e., the black region in Fig. 2f). A background mask was then defined as the inverse of the background segment (Fig. 2g). The original thresholded image (Fig. 2c) was then background-corrected by multiplying it by the binary background mask. This multiplication effectively acts as a Boolean "and" operator, with True(1) products corresponding to foreground and False(0) products corresponding to background. Cells were counted from the background-corrected image by identifying blobs using the "Laplacian of Gaussian" method. All automated counts were checked by plotting the locations of counted cells over the original images (Fig. 2h).

Method 2: Modification of "traditional" ImageJ cell counting method (Bankhead 2013)

Unprocessed RGB images were converted to binary masks and subjected to background and cell fluorescence analysis as described above for manual ImageJ micrograph measurements, except a controlled blur (Gaussian Blur filter, $\sigma = 2$) was applied in lieu of manually adjusting the threshold for each image after default thresholding. Blurred masks were then converted to binary masks. The same raw Cy5 630X magnification image as Fig. 2a is shown in Fig. 3a, while Fig. 3b shows the image mask.

Method 3: Modified "broad pass—fine pass" version of ImageJ cell counting

To create a final binary mask that accurately replicated all cells in a micrograph for fluorescence measurements and cell counting, we designed an alternative ImageJ "two-pass" approach, using a "broad-pass" and a "fine-pass" mask, as no single set of conditions was universally appropriate for all cells in an image.

The "broad pass" binary mask was created using the same background subtraction and blurring procedure as in Method
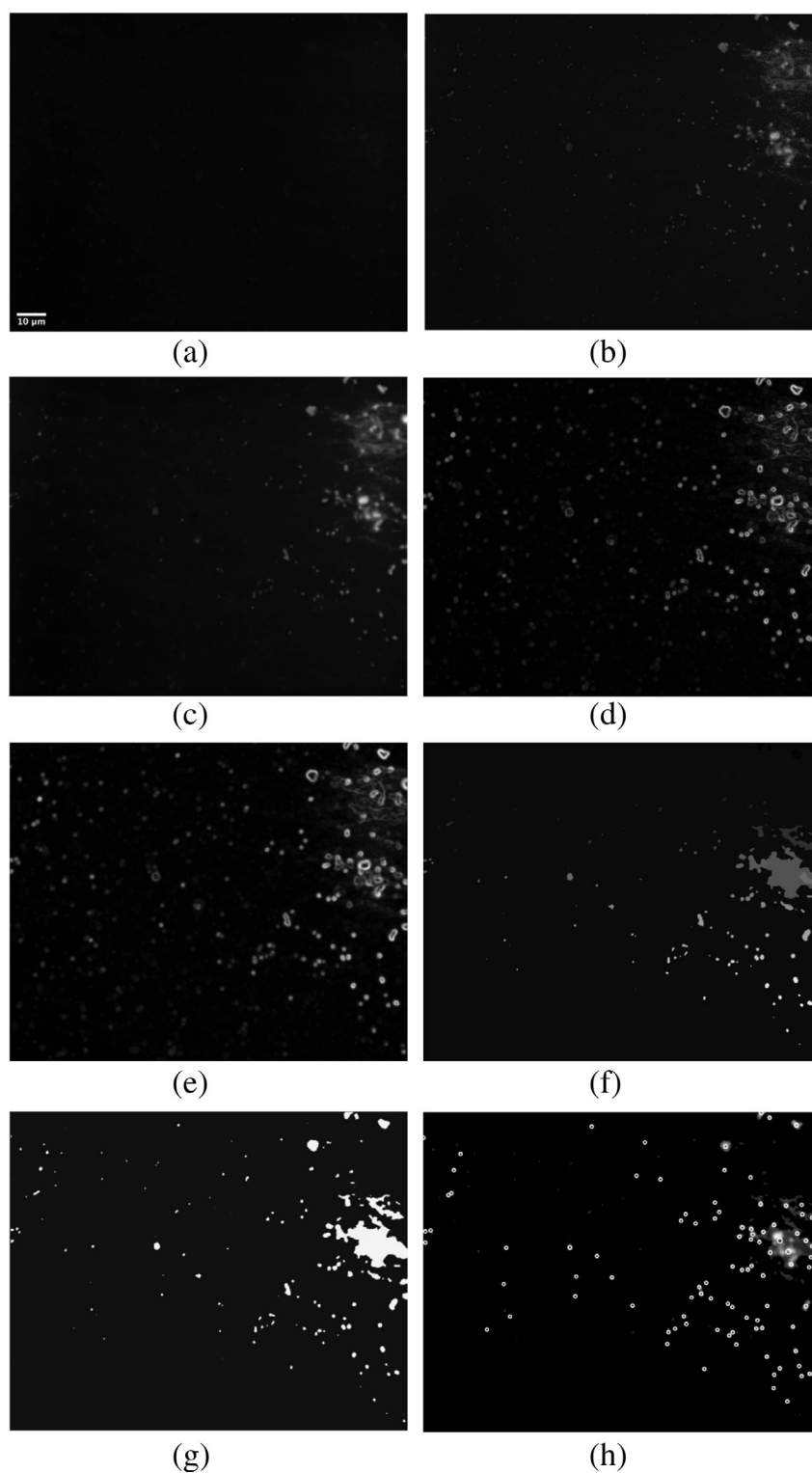
Fig 2. Step-by-step outputs of Method 1 as applied to a micrograph of a FGLsample (depth = 20.5 m) hybridized against Cy5-Eps682 after 2.0 mM CuSO$_4$/EtOH treatment. Original image was acquired after 2 min camera exposure through a 63X objective lens using Cy5 filter set illumination. (**a**) Unprocessed original image, (**b**) after histogram matching, (**c**) after dynamic thresholding, (**d**) after applying Sobel filter, (**e**) after applying Gaussian blur, (**f**) after applying watershed, (**g**) after applying background mask, (**h**) circles of the locations of cells detected by "Laplacian of Gaussian" method are drawn over the background-corrected image.

(a)   (b)

(c)   (d)

(e)   (f)
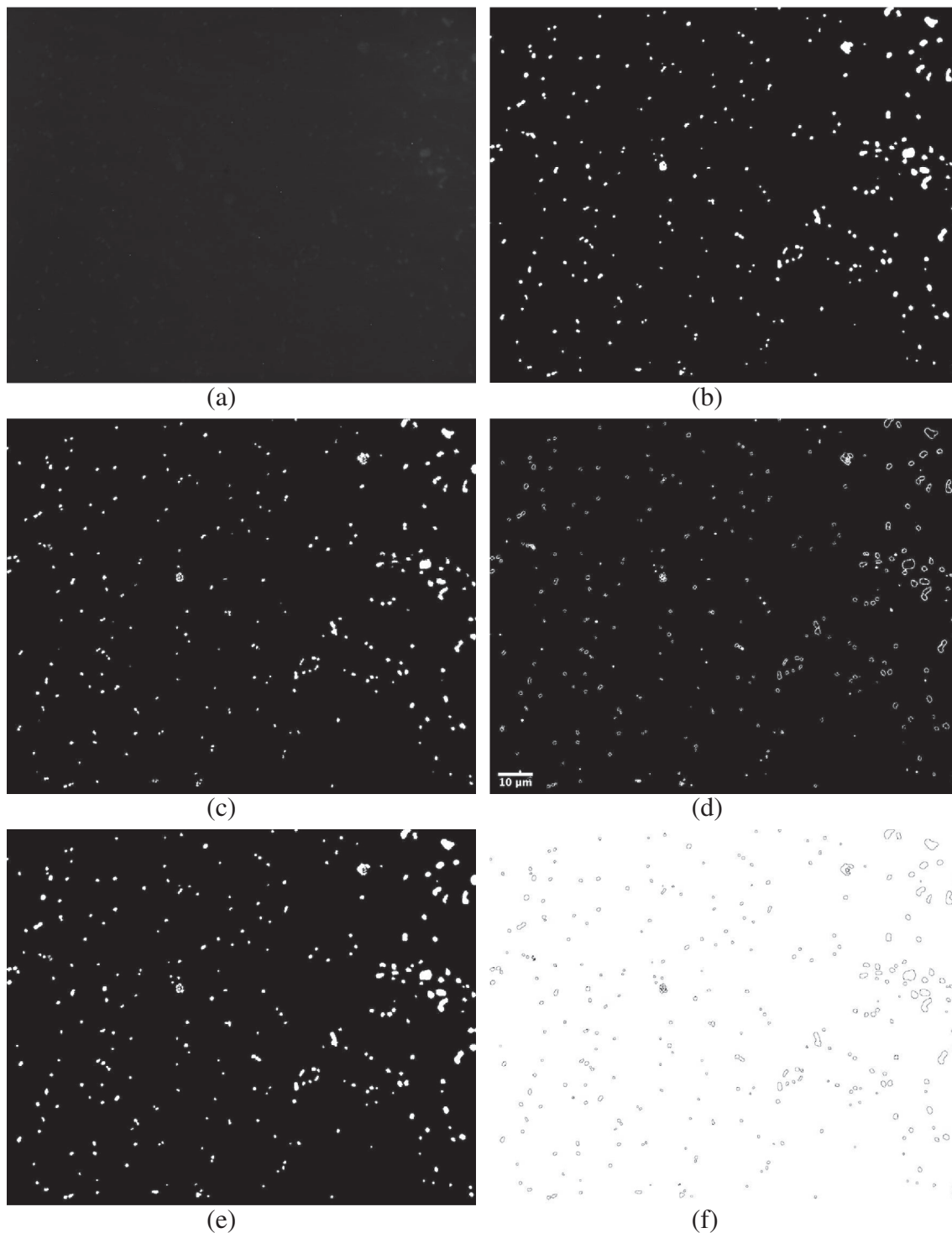
Fig 3. Step-by-step outputs of Methods 2 and 3 (*see* text) as applied to a micrograph of a FGL sample (depth = 20.5 m) hybridized with Cy5-Eps682 after treatment with 2.0 mM CuSO$_4$/EtOH. Original image was captured after 2 min camera exposure through a 63X objective lens using Cy5 filter set illumination. (**a**) Original image, (**b**) the broad-pass mask, (**c**) the fine-pass mask, (**d**) the XOR mask, (**e**) the final mask, and (**f**) the outlines of cells detected by the ImageJ "analyze particles" function after the application of all masks.

2 (Fig. 3b). Using the "Analyze Particles" function, particles detected by the broad-pass mask were added to the ROI Manager, but count information was discarded by choosing not to

display the "Results" data table. Background of the background-corrected RGB image, found in Method 2, was defined as the inverse of the combined broad-pass particle

selection. This background selection was then flooded with pure black, effectively removing the background from the image. The flooded RGB was then converted to a "fine pass" binary mask without speckling that rendered cell boundaries more accurately (Fig. 3c). To combine the unique features of both masks into a final binary mask, the exclusive-or (XOR) Image Calculator function was applied to broad- and fine-pass masks. The resulting binary image showed cells unique to each mask (filled) and redundant cells (unfilled) (Fig. 3d). Cells missed by the fine-pass filter (filled cells) were then added back into the fine-pass mask to create the final mask (Fig. 3e). Cells in the final mask were added to the ROI manager using the "Analyze Particles" function, selecting not to display the "Results" data table. Example code is presented in Supplemental Materials (Method 3 codes).

ROIs added to the ROI manager from the final mask in both ImageJ methods were used to select and measure integrated density, scaled area, and mean gray-scale values of either the combined area of all cells or individual cells (depending on sample type and analysis goal) and the original 16-bit RGB image's background. Cell and background "Results" tables were saved. Resulting data were used to calculate the background-corrected cell fluorescence intensity per cell area f_c (fluorescence intensity as pixel gray value/μm^2) of the combined cell area or each cell in a given image. The f_c of the combined cell area of CuSO$_4$/EtOH-treated unhybridized samples served as a threshold for separating autofluorescent cells from target cells for each set of microscope illumination filters by individual cell fluorescence measurements. Cell data tables from each image of a CuSO$_4$/EtOH-treated, hybridized sample were filtered to retain only cells with an f_c two standard deviations greater than the threshold. Filtered data from all 15–20 images of the sample were used to calculate its average true hybridized cell concentration and standard deviation, with each image being treated as an analytical replicate. A detailed explanation of this procedure and a recommended algorithm for high-throughput data filtration is provided in Supplemental Materials (Explanation of Method 3 data outputs and data filtration).

Assessment and discussion

First, we will assess the sample size (number of micrographs) required for minimizing analytical uncertainty (RSD = relative standard deviation) of fluorescent cell counts, f_c and g_b. Using manual image analysis results as our benchmark, we will then evaluate which automated method most accurately measured cell and background area, integrated density, mean gray values, f_c, g_b and therefore the derived cell counts. We then establish why a chemical pretreatment is required to accurately enumerate probe-positive cells rather than simply subtracting average autofluorescent cell counts. Autofluorescence suppression pretreatments are then compared for their ability to reduce brightness of autofluorescent cells and limit background fluorescence while retaining the FISH signal. Finally, we present a profile of Eps682-hybridized cell abundances using the most successful treatment and image processing methods and compare their community representation (% of DAPI cells) to those from other low-oxygen water column environments.

Sample size

For our field sample with the most heterogeneous distribution and cell aggregation (20.5 m), counting error was predictably higher (RSD $\cong$ 30%) than in more homogeneous samples. Typically, 15–20 micrographs of a given sample is sufficient to asymptotically approach a minimum RSD of $\sim$ 10%. Analyzing more fields-of-view may marginally reduce analytical uncertainty, but at a significant cost in the time needed for analysis (Kirchman et al. 1982; Muthukrishnan et al. 2017). Nevertheless, to determine if analytical uncertainty in cell counts for our problematic samples could be reduced, we enumerated all cells in our most problematic sample (20.5 m) in 20 images and compared micrographs captured at 1000X magnification to 630X images which integrate more of the variability in cell distributions on the filter. The 630X images yielded RSDs that were 5–10% lower than those calculated from 1000X images (RSD = 15–25%). However, increasing the number of analyzed images beyond 20 did not appreciably reduce analytical uncertainty beyond $\sim$ 5%. After data filtration the RSD of true hybridized cells is approximately 10% greater than total cells because they are less abundant, so that smaller differences between fields of view result in a greater RSD. The cell and background fluorescence (f_c and b_g, respectively) were more consistent than cell counts among micrographs from a given sample. Even for our problematic sample, RSDs of f_c and b_g were minimized to 3 and 5% after measuring only three micrographs through the Cy5 filter set. RSDs of f_c and b_g were higher when measured through the Cy3 filter; 3 fields of view yielded RSDs of 8 and 28%, respectively.

Cell-counting and fluorescence measurement methods

Of the three automated image analysis approaches, Method 3 was the only one to produce cell and background fluorescence measurements, and ultimately, cell counts that consistently agreed with manual measurements of fluorescent cells within analytical uncertainty (Fig. 4). Method 3 produced a mask that retained distinct cell boundaries, as with the local Bernsen thresholding, but without the trade-off of overlooking a significant number of cells; although, some fidelity was still lost in rendering cell boundaries (Fig. 5). Method 3 was also adept at defining cell boundaries of clumped/aggregated cells (Fig. 6). Nearly identical f_c data for both Cy3 and Cy5 labeled samples generated manually and automatically demonstrate that Method 3 accurately measures fluorescence as well as cell counts (Table 2).

For Methods 2 and 3, we found that ImageJ global "Default" thresholding was superior to other ImageJ
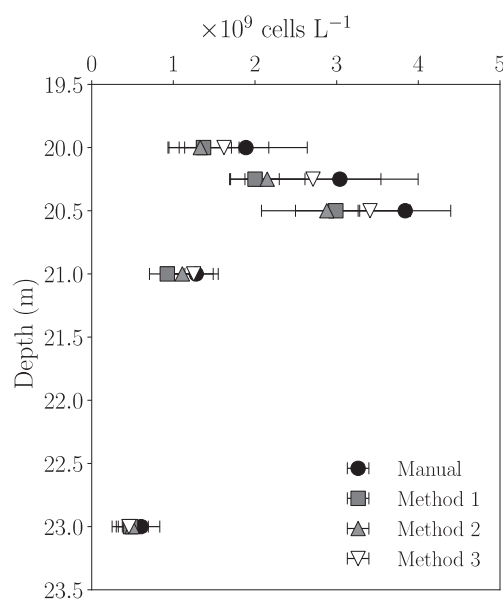
Fig 4. Concentrations of putative probe-positive prokaryotes determined by manual counts (black circles) or by automated Methods 1 (dark gray squares), 2 (gray upward triangles), and 3 (white downward triangles) from untreated FGL samples hybridized against Cy5-Eps682. Micrographs were imaged through a 63X objective lens using Cy5 filter set illumination. Symbols and horizontal bars represent averages and standard deviations.

thresholding methods that have been suggested for cell enumeration routines. ImageJ global Otsu and local Bernsen thresholding methods were recommended by Nichele et al. (2020) for a cell analysis routine to resolve cell merging and resulting undercounting (as observed using our Method 2). We found that thresholding using global Otsu thresholding identified most cells, but aggregated closely-spaced cells, resulting in undercounting. This problem has been reported before and is caused by the method's over-estimation of the threshold (Dima et al. 2011). In contrast, local Bernsen thresholding was able to identify closely-spaced cells but did not identify many other cells (Fig. 5).

The Python counting method (Method 1) worked as well as Method 3 on micrographs captured at both 630X and 1000X magnification, if cells were not crowded together. Over-crowding, especially at lower magnifications, makes cell boundaries more difficult to resolve (Fig. 7). Therefore, the Python method counted cells inaccurately in micrographs of our high cell density samples with aggregated cells when 630X magnification was chosen to reduce analytical uncertainty of the census. The traditional ImageJ method (Method 2) undercounted by 30% on average compared to manual counts at either magnification, regardless of image conditions, due to its merging of closely-spaced cells (Fig. 7). Cell merging was exacerbated by the necessity of applying a Gaussian blur in lieu of the ability to adjust the threshold for every micrograph. Without the blur, speckling/noise in the background of

automatically thresholded images resulted in unusable binary masks even after applying the "Despeckle" function. More-over, some cells with less defined boundaries shrunk in the mask and were excluded by the "Analyze Particles" routine detailed above in the manual micrograph analysis section.

Elimination of autofluorescence by subtraction

FISH probe-positive cell concentrations were calculated for a given sample by subtracting the average autofluorescent cell concentrations (manual counts from untreated unhybridized subsample) from the concentrations of total fluorescent cells (Eps682 probe-positive + autofluorescent cells) counted in untreated subsamples. Calculating Eps682 cell concentrations simply by subtraction in this manner was problematic. Using Method 3, our most accurate automated counting method, produced the greatest number of discrete samples in the profile with average Eps682 concentrations greater than zero. Even so, because autofluorescent prokaryotes made up more than half of DAPI-stainable cells in some FGL samples (e.g., 10b), calculated differences between those cells and total fluorescent cells (autofluorescent and hybridized) when enumerating less abundant FISH probe targets can be exceedingly small.

With cell counting RSDs seldom as low as 10% for a single target, errors propagated from independent cell counts of two or more targets can be larger than real differences among targets. In fact, apparent concentrations calculated by difference can be negative in many cases which is a physical impossibility (Fig. 8). Therefore, true concentrations of the hybridized cells are poorly constrained and the entire profile shape is dubious. This illustrates that determining FISH-positive cell concentrations by difference in an autofluorescent sample without an autofluorescence suppression treatment is inappropriate for determining concentrations of lower abundance taxa by FISH, especially in aquatic systems subject to CyanoHABs.

Elimination of autofluorescence by sample pretreatment

Clearly, accurate enumeration of FISH-positive cells from samples with cyanobacteria cells benefits from autofluorescence suppression prior to image acquisition. Furthermore, FISH should be performed using a fluorophore that is visible through a filter set that yields the least autofluorescence and best micrograph quality. Therefore, we evaluated the performance of previously published autofluorescence suppression pretreatments on our challenging FGL samples, several FISH fluorophores, and three automated image analyses routines.

We first applied a chemiphotobleaching protocol developed in our lab to prepare algal cells for Raman microspectroscopic interrogation (Yakubovskaya et al. 2019). In FGL samples from the depths of highest cyanobacterial abundances, autofluorescence was not effectively removed from preparations using this treatment as examined by fluorescence microscopy through the FITC, Cy3 and Cy5 filter sets, even
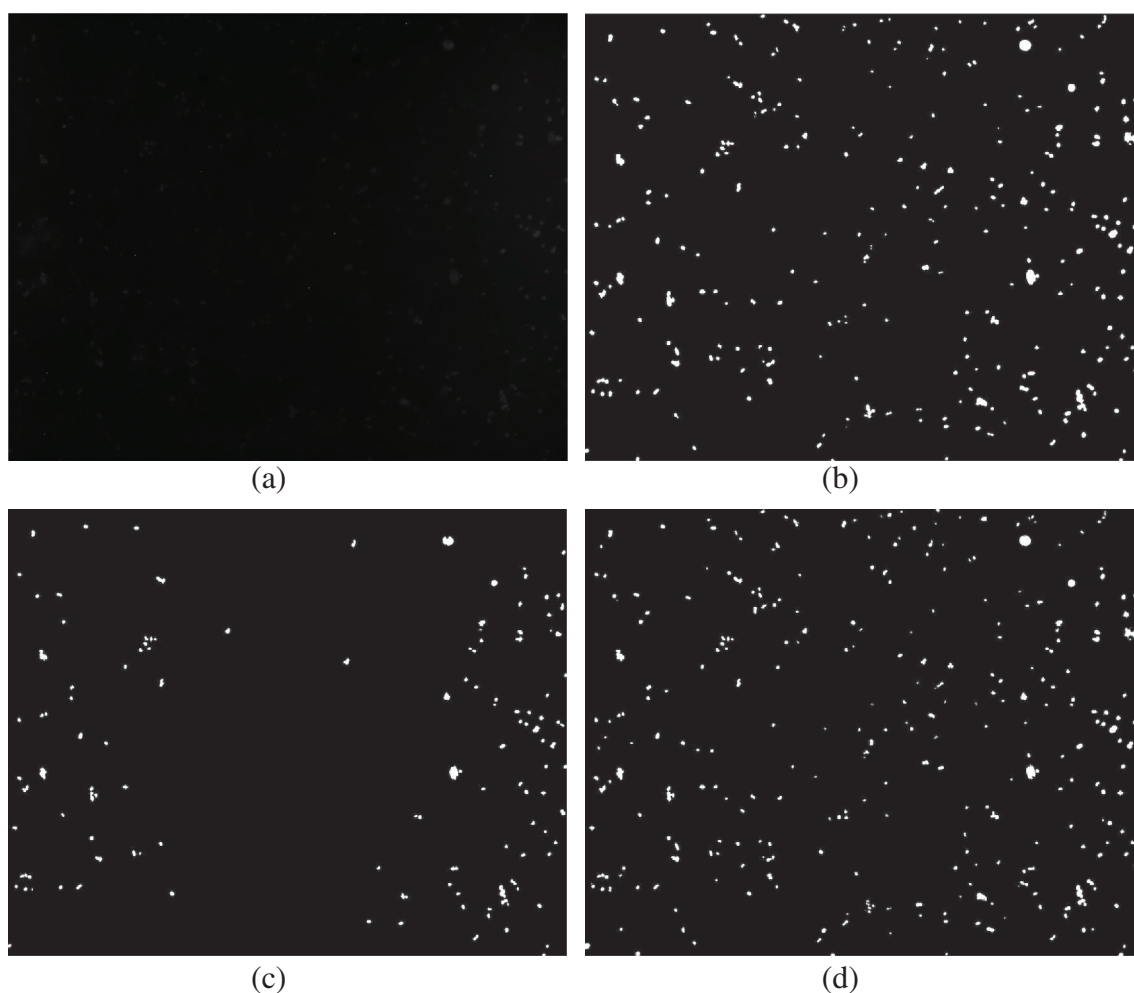
Fig 5. A comparison of the masks produced by Otsu thresholding, Bernsen thresholding, and Method 3 as applied to a micrograph of a FGL sample (depth = 20.5 m) hybridized against Cy5-Eps682 after treatment with 2.0 mM CuSO$_4$/EtOH. Original image was captured after 2 min camera exposure through a 63X objective lens using Cy5 filter set illumination. (**a**) original image, (**b**) image after Otsu global thresholding, (**c**) image after Bernsen local thresholding, and (**d**) the image after Method 3.
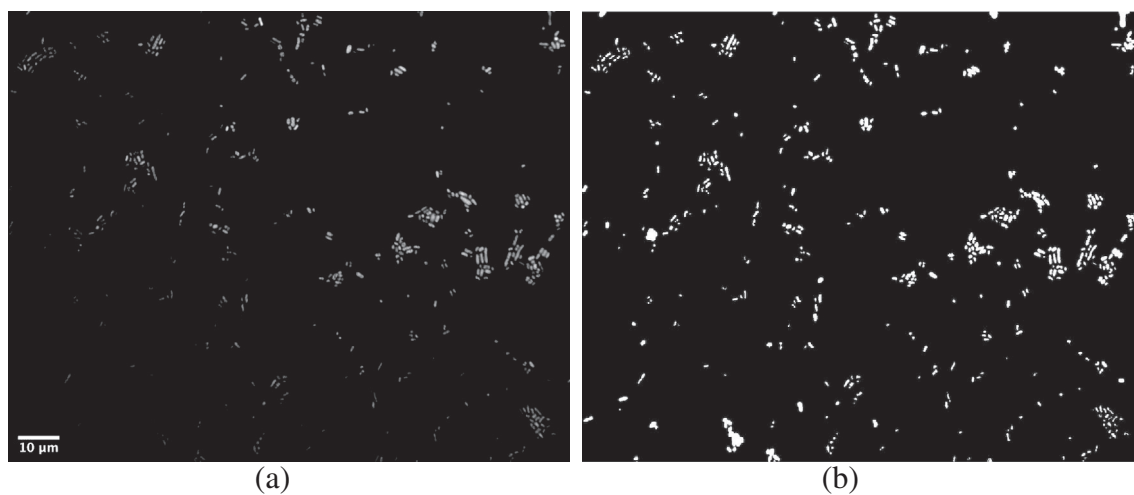
Fig 6. (**a**) An unprocessed micrograph of DAPI-stained *E. coli* cells observed at 630X magnification, and (**b**) the same image after processing by Method 3.

after 24 h treatments. We speculate that extracellular materials in the FGL samples, such as transparent exopolymeric substances (TEPs) or suspended mineral matrices, could either

Table 2. Comparison of manually and automatically generated f_c (background-corrected cell fluorescence intensity measured as pixel gray value/μm^2) and g_b (average background fluorescence intensity measured as pixel gray value/μm^2) of 2 mM CuSO$_4$/EtOH-treated unhybridized samples for Cy3 and Cy5 filter sets by Methods 2 and 3.

Method	Filter set	f_c	g_b
Manual	Cy5	4.39	3.14
Method 2	Cy5	5.17	3.15
Method 3	Cy5	4.48	3.14
Manual	Cy3	39.5	27.9
Method 2	Cy3	45.4	28.5
Method 3	Cy3	38.3	36.3

exhaust most of the peroxide's oxidation potential or formed a protective barrier around cells. The chemiphotobleaching protocol relies on light-enhanced chemical oxidation by 3% H$_2$O$_2$, and the reaction efficiency increases exponentially with light irradiances, which varies both with the light source's intensity and with proximity to the sample (Yakubovskaya et al. 2019). If an overlying matrix were thick enough or pigmented, the amount of light reaching autofluorescent cells could be significantly attenuated.

The second pretreatment evaluated was more successful and involved brief immersions of samples in CuSO$_4$ solutions followed by immersion in EtOH. This method works by dissociated Cu^{+2} ions diffusing into cells and exchanging with pigment metals (e.g., Mg^{++}, Fe^{++}, Mn^{++}), which then go into solution. Those metals, along with intact EtOH-soluble pigments (e.g., chlorophylls, carotenoids), are then washed away in the EtOH rinse step (Zeller et al. 2016). Mineral matrices or extracellular substances would likely not interfere with this method, because it works by diffusion and ionic exchange
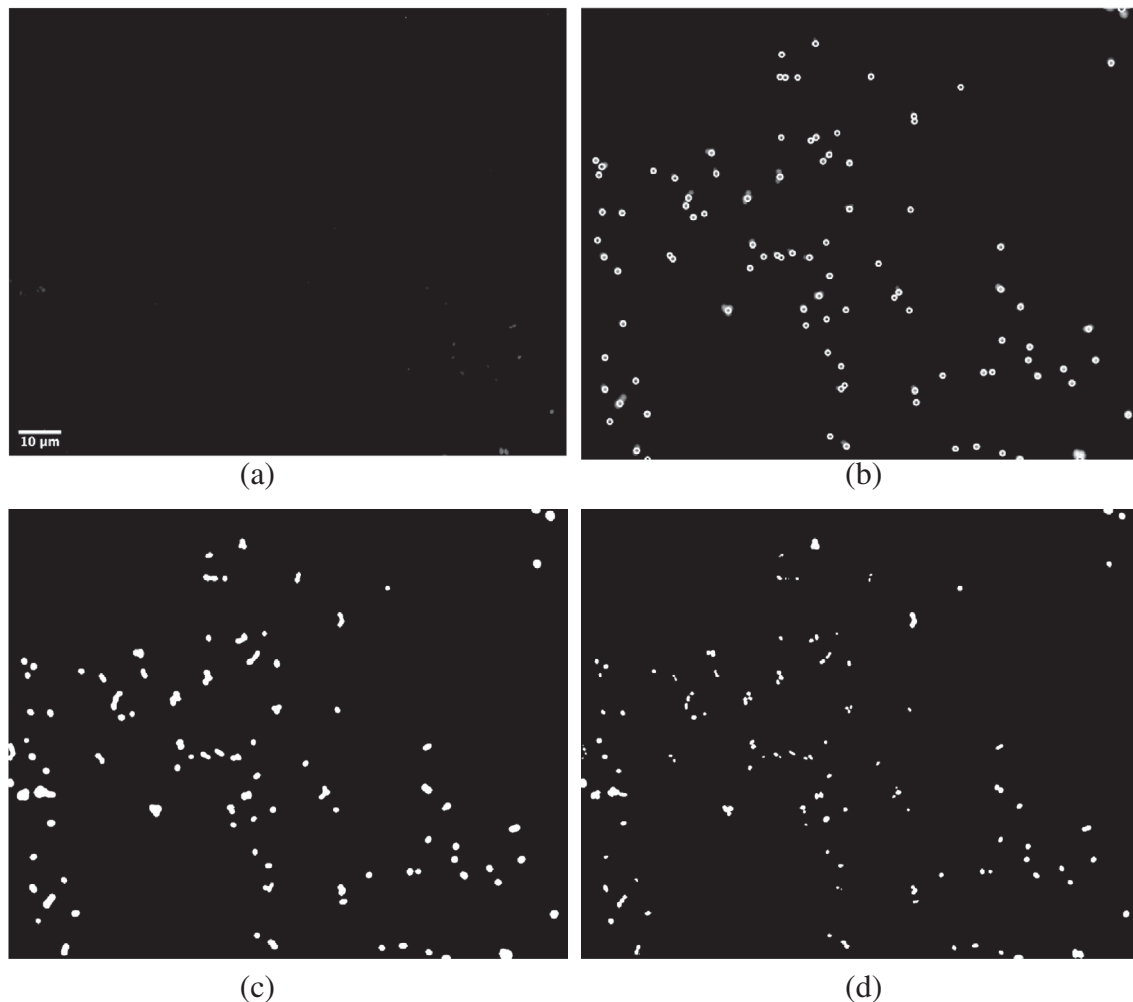
Fig 7. Image processing of an untreated FGL sample (depth = 20 m) hybridized with Cy5-Eps682 at 1000X magnification. Shown are (**a**) the unprocessed 16-bit image, and after processing with (**b**) Method 1, (**c**) Method 2, and (**d**) Method 3.

rather than the light exposure-dependent oxidation potential of the chemiphotobleaching method.

To determine optimal $CuSO_4$ exposure, three different concentrations were tested on unhybridized samples and DAPI counterstaining was applied before and after each treatment. DAPI cell and background fluorescence levels were comparable to untreated controls when DAPI counterstaining was performed after $CuSO_4$ treatment (Table 3). Among 1.29, 2.0, and 4.0 mM solutions, 2.0 mM $CuSO_4$ produced the best images.
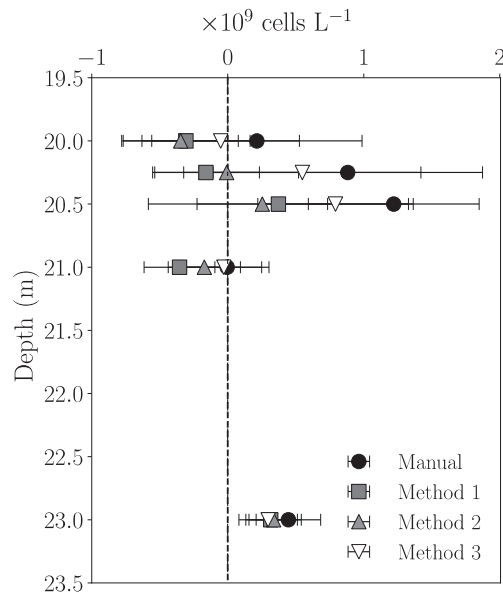
Fig 8. Apparent concentrations of epsilonbacteraeota cells in the FGL water column determined by difference. Concentrations were calculated by subtracting manually-counted total autofluorescent cells from corresponding samples hybridized with the Cy5-Eps682 FISH probe, but not pretreated with 2.0 mM $CuSO_4$/EtOH. Cells in hybridized samples were enumerated either manually (black circle) or by Method 1 (dark gray square), Method 2 (gray upward triangle), or Method 3 (white downward triangle). Symbols and horizontal bars represent averages and propagated standard deviations.

Increasing the concentration of $CuSO_4$ from 1.29 mM to 2.0 mM suppressed cell autofluorescence measured through all microscope filter sets but increasing the $CuSO_4$ concentration to 4.0 mM worsened background fluorescence to the point where micrographs could not be analyzed (Table 3). We are not certain why the 4.0 mM $CuSO_4$ solution worsened the background fluorescence. $CuSO_4$ has been reported to destroy bacterial cell membranes by interacting with lipids and to form copper residues in sediment when used as a commercial algaecide (Kansole and Lin 2017). However, lysed cells do not lose much rRNA. In fact, repeated freezing and thawing and enzyme treatments to encourage cell lysis are often used in FISH protocols to facilitate better probe delivery. It is possible that at some critical concentration, copper residues could form on the filters, which would in turn increase the divalent salt concentration in the hybridization buffer. If so, the melting temperature of the FISH probe would increase, resulting poor hybridization and therefore preparations with high background fluorescence from unbound probe.

Micrographs of 2.0 mM $CuSO_4$/EtOH-treated unhybridized samples imaged through the Cy5 filter set were superior to those imaged through Cy3 and FITC filter sets in terms of cell and background fluorescence relative to untreated control samples. Background fluorescence observed through the Cy3 and FITC filter sets intensified substantially after $CuSO_4$/EtOH treatment, while background fluorescence through the Cy5 filter set was reduced by 52.1 to 57.6% (average = 55.3%) (Table 3). Background fluorescence of micrographs from pretreated samples imaged through the Cy3 and FITC filter sets created widespread speckling during image processing in ImageJ, which in turn obscured the cells once the image was converted to a binary mask. It is unclear why this occurs, but we speculate that it may relate to the broader excitation and emission spectral ranges of Cy3 and FITC filter sets transmitting more background radiation (noise) than Cy5.

Once the optimal concentration of the $CuSO_4$ was established, we determined when to apply the chemical

Table 3. Average f_c (background-corrected cell fluorescence as pixel gray value μm^{-2}) and average background fluorescence as mean pixel gray value μm^{-2} (g_b) of unhybridized samples $CuSO_4$/EtOH-treated with either 1.29 or 2.0 mM $CuSO_4$ (details in Materials and methods) as measured through DAPI, Cy3, Cy5, and FITC filter sets. Presented are the f_c of the $CuSO_4$/EtOH-treated sample, the f_c as a percentage of the average f_c of untreated unhybridized samples, and g_b of the $CuSO_4$/EtOH-treated sample as a percent of the average g_b of untreated unhybridized samples. (Note: Samples treated with 6 μM $CuSO_4$ are omitted because excessive background fluorescence precluded measuring f_c and g_b).

Filter set	1.29 mM CuSO₄			2.0 mM CuSO₄		
	f_c	f_c (% of control)	g_b (% of control)	f_c	f_c (% of control)	g_b (% of control)
DAPI*	9.0/22.3	28.5/103.7	196.3/335.9	19.3/21.0	61.2/97.6	177.6/132.2
Cy3	42.6	24.8	436.1	39.5	21.0	384.3
Cy5	5.1	3.3	49.7	4.5	2.9	42.0
FITC	ND	ND	ND	8.5	14.8	143.0

*Formatting stained before/after $CuSO_4$ treatment.

pretreatment relative to the FISH procedure. To quantify the effectiveness of pretreatments for image analysis, we now define several indices. The signal-to-noise ratio (S/N) is the ratio of the f_c of hybridized samples to the f_c of unhybridized samples after both were CuSO$_4$/EtOH-treated. The signal-to-background ratio (S/B) is the ratio of the f_c of CuSO$_4$/EtOH-treated hybridized samples to the g_b in the same sample. The background-to-noise ratio B/N is the ratio of the g_b in CuSO$_4$/EtOH-treated hybridized samples to f_c of CuSO$_4$/EtOH-treated unhybridized samples.

The f_c values calculated from Cy3 and Cy5 micrographs were slightly higher when 2.0 mM CuSO$_4$/EtOH treatment is applied before hybridization rather than after as practiced by Zeller et al. (2016) (Table 4). Cy5 and Cy3 f_c values of truly hybridized cells (cells with an f_c > average residual autofluorescence ≥2 *SD*) were 3.0 and 2.5 times higher, respectively, than residual autofluorescence in unhybridized samples after treatment. This means hybridized cells can be confidently distinguished from autofluorescent cells by their fluorescence intensity when enumerating. *S/B*, *S/N*, and *B/N* ratios of Cy5 and Cy3 probes were comparable if the 2.0 mM CuSO$_4$/EtOH treatment was applied before hybridization, but the Cy5 probe performed significantly better than the Cy3 probe if the CuSO$_4$/EtOH treatment was applied after hybridization in terms of *S/B* and *B/N* (Table 4). A high *S/B* ratio is necessary to clearly distinguish cells (foreground) from the background during image analysis. The higher the *B/N*, the less likely it is for the image analysis routine to capture residual autofluorescent cells because they will blend more into the background.

When samples were hybridized with Cy3 probes either before or after CuSO$_4$/EtOH treatment, it was difficult to measure cell and background mean gray value, area, and integrated density due to intensified background fluorescence. As a result, f_c, g_b, and cell concentrations were difficult to calculate (Table 3). In a batch of 396 (1 Cy3 : 1 Cy5) micrographs run through Method 3, all of the 143 images with mottled cell masks (and resulting erroneous count data) were Cy3, accounting for 72% of all Cy3 input images. Cy3 hybridizations that were 2.0 mM CuSO$_4$/EtOH-treated prior to FISH had a significantly higher success rate than those CuSO$_4$/EtOH-treated after (80% vs. 20%). Overall, due to higher *S/N* and f_c in all channels, application of the CuSO$_4$/EtOH treatment

prior to FISH yielded more desirable results than post-hybridization application as recommended by Zeller et al. (2016).

To demonstrate that the 2.0 mM CuSO$_4$/EtOH treatment did not compromise oligo-FISH performance, we applied the treatment before and after hybridizing filters with *E. coli* cells against Cy5-Gam42a and Bet42a, along with an untreated *E. coli* filter that served as a control. On filter wedges treated with 2.0 mM CuSO$_4$/EtOH, all DAPI counterstained cells completely coincided with hybridized cells in the same field-of-view. Therefore, we conclude that the chemical pretreatment did not negatively affect probe hybridization efficiency with *E. coli* cells. *S/B* and f_c were lower if the CuSO$_4$/EtOH treatment was applied after oligo-FISH, as with lacustrine samples. The *E. coli* f_c was also sufficiently higher (>2×) than mean residual Cy5 autofluorescence (+2 SD) of our treated unhybridized lacustrine lake water samples. We view this as proof-of-concept that true Cy5 hybridization signals can be reliably distinguished from residual autofluorescence (Table 5).

As with our environmental samples, the 2.0 mM CuSO$_4$/EtOH treatment did not affect the DAPI counterstaining of *E. coli* cells when applied after the 2.0 mM CuSO$_4$/EtOH treatment and FISH. Fluorescence intensity per cell area (f_c) of DAPI-stained *E. coli* cells was consistently threefold greater than cells in lacustrine samples, but this could be because the *E. coli* was stained immediately after harvesting cells, fixing, and freezing while the environmental samples were fixed and frozen for 2 years prior to these measurements. Even stored at −20°C, cells do gradually degrade over longer periods of time. Alternatively, it could be because all *E. coli* were harvested during their exponential growth stage and were likely to be DNA-rich, whereas environmental samples contain a mixture of cells in various growth phases (Aviv et al. 1996). Cells that are in their stationary growth phase shut off their ribosomal RNA promoters, which ultimately disrupts protein synthesis and causes cell degradation (Aviv et al. 1996; Lodish et al. 2000). It is plausible that if cells are degraded in this way, or have less DNA overall, DAPI staining may be dimmer.

Data generated using image analysis Method 3 after the 2.0 mM CuSO$_4$/EtOH pretreatment procedure still needed to be cleaned using the appropriate residual autofluorescence

Table 4. Signal-to-noise (S/N), signal-to-background (S/B), and background-to-noise (B/N) ratios of hybridized samples after 2.0 mM CuSO$_4$/EtOH treatment after filtering data (retaining only cells with an f_c > average residual autofluorescence + 2 f_c).

Filter	2.0 mM CuSO$_4$ before				2.0 mM CuSO$_4$ after			
	S/N	*S/B*	*B/N*	f_c	*S/N*	*S/B*	*B/N*	f_c
DAPI	N/A	0.93	N/A	21.0	N/A	0.68	N/A	19.3
Cy3	2.8	3.2	0.93	112.6	2.6	1.9	1.4	102.0
Cy5	3.1	2.9	1.2	13.7	2.9	4.1	0.72	12.8

threshold. Without removing subthreshold cells from data tables, a substantial number of false Eps682-positive cells remained, albeit fewer than in untreated samples. These false positives resulted in overestimated Eps682 cell concentrations compared to estimates derived from differences between autofluorescent cells and untreated, hybridized samples. Once the data table for each micrograph was culled to exclude cells with an f_c value less than two standard deviations above the average residual autofluorescence, the resulting Eps682 cell concentrations agreed with the by-difference estimated concentrations (Fig. 9a). The average f_c of ~ 8 for unfiltered data reflected a mixture of hybridized cells and residual autofluorescence. The 2 SD cut-off yielded hybridized cell f_c's of about 10–12, which is the same as the f_c for cultured *E. coli* cells, and residual autofluorescent cell f_c's ~ 4.5, agreeing with the 2.0 mM CuSO$_4$/EtOH-treated unhybridized samples.

True Eps682-positive cells accounted for 15% of DAPI stainable cells at the depth of their maximum relative abundance (Fig. 9b). This relative abundance is similar to the maximum relative abundances reported in other anoxic/euxinic water columns (e.g., Cariaco Basin, Black Sea, Farö Deep, Gotland Deep) (Lin et al. 2006; Grote et al. 2007). To validate the chemical treatment and data filtration routines, we repeated the procedure using a Cy3-labeled version of the same probe and manual ImageJ analysis on our 20.5 m sample. We found that the results agreed with Cy5 counts within analytical uncertainty, demonstrating that even using two different fluorophores with different autofluorescence cut-offs and different enumeration methods, the 2.0 mM CuSO$_4$/EtOH treatment and data filtration protocol still independently produce equivalent means and analytical uncertainty (6.78 ± 2.40 vs. $7.06 \pm 2.53 \times 10^8$ cells L^{-1} for Cy5 and Cy3, respectively).

Table 5. *E. coli* pure culture controls hybridized with Cy5-labeled Gam42a and imaged through DAPI and Cy5 filter sets. Signal to background ratios (*S/B*), f_c for samples imaged with the DAPI filter set, and the *S/B*, f_c, and percent overlap with DAPI cells are presented for the same sample fields-of-view imaged with the Cy5 filter set.

Treatment	DAPI		Cy5		
	S/B	f_c	*S/B*	f_c	% overlap with DAPI cells
None	5.4	62.3	3.7	10.8	100
2.0 mM CuSO$_4$ before	6.1	66.1	4.7	13.1	100
2.0 mM CuSO$_4$ after	5.5	63.7	3.3	10.1	100
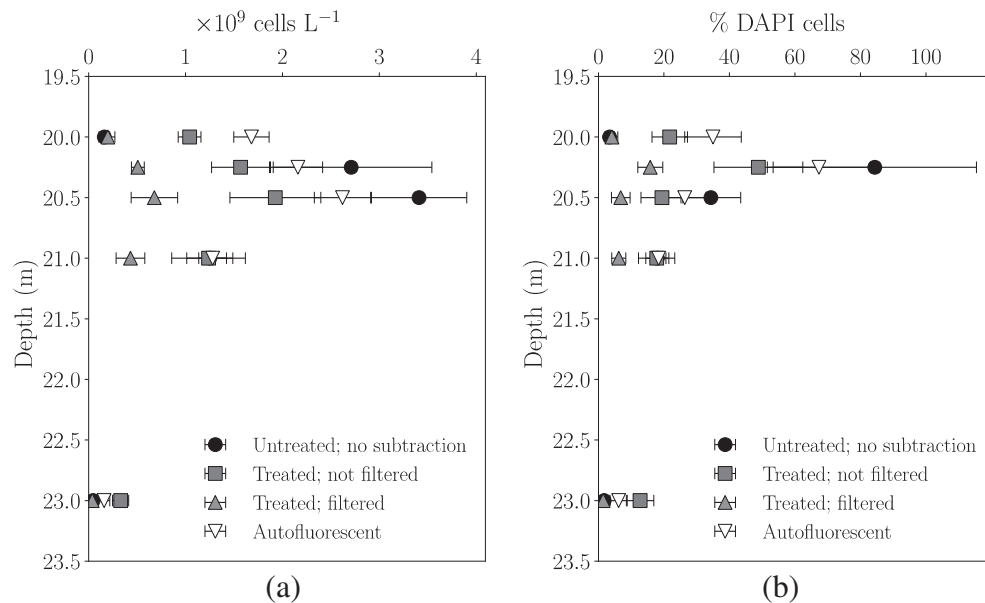
Fig 9. (**a**) Concentrations of fluorescent prokaryotic cells imaged through the Cy5 filter set that: were not pretreated but were hybridized with Cy5-Eps682 (black circles); pretreated with 2.0 mM CuSO$_4$/EtOH and hybridized with Cy5-Eps682 but without data filtration (dark gray square); pretreated with 2.0 mM CuSO$_4$/EtOH and hybridized with Cy5-Eps682 with data clean up (gray upward triangle); not treated with 2.0 mM CuSO$_4$/EtOH nor hybridized with Cy5-Eps682 or (white downward triangle); (**b**) the same data as (**a**) presented as a percent of DAPI-positive cells in the same samples.

Closing remarks and recommendations

To reduce cyanobacterial autofluorescence in environmental samples and remove residual autofluorescence from image analysis data, we have established a method utilizing chemical pretreatment with 2.0 mM CuSO$_4$/EtOH and automated image analysis using the Fiji distribution of ImageJ. The protocol should be performed in the following order: chemical pretreatment, FISH using Cy5 labeled probes, DAPI counterstaining, and mounting with a 4 : 1 mixture of Citifluor™: Vectashield® mounting solutions. At least 20 monochrome images should be acquired from each sample in the red channel (although an IR cut may be fine with newer cameras) at the magnification that results in the best resolution of target cells and lowest counting variability (analytical uncertainty), and processed using the steps detailed in Method 3 followed by data filtration. This final workflow is summarized in Fig. 10. We note, in particular, that in our hands applying the chemical pretreatment prior to FISH produced higher quality images than those produced using Zeller et al.'s (2016) original protocol. We found that our protocol increased signal-to-noise and signal-to-background ratios of hybridized samples and greatly decreased autofluorescence of nontarget cells relative to untreated control samples imaged through all fluorescence microscopy filter sets. However, the background fluorescence in the Cy5 excitation–emission spectral range was substantially lower relative to untreated controls, making Cy5 the highly preferable fluorophore for automated analysis.

Using the Eps682 FISH probe, we demonstrated that our method is sensitive enough to enumerate a clade which typically has low relative abundances compared to other common FISH targets (e.g., Alpha-, Delta-, and Gammaproteobacteria). The method presented in this paper is inexpensive and relatively straightforward for anyone already performing FISH studies of aquatic systems. We also found that the image analysis component of our method is useful as an independent tool for several other applications. It was able to accurately enumerate densely populated micrographs of samples' DAPI counterstained cells and therefore can be used for high-throughput automated total cell counts. Because it is able to associate fluorescence intensity data with individual cells, it is also an ideal tool for quantitatively comparing the fluorescence intensity of probe-positive cells that have been hybridized using different buffer stringencies when optimizing hybridization buffer chemistry for a FISH probe.

However, there are some limitations to our method. Due to the low fluorescence intensities of the Cy5 fluorophore, it is time consuming to take 20 micrographs per sample at 2-min exposure times. This method also requires that the exposure time, lamp intensity, and magnification for all micrographs of a given sample remain the same as unhybridized CuSO$_4$/EtOH-treated autofluorescence controls. If, for example, the microscope mercury lamp is nearing the end of its lifespan,
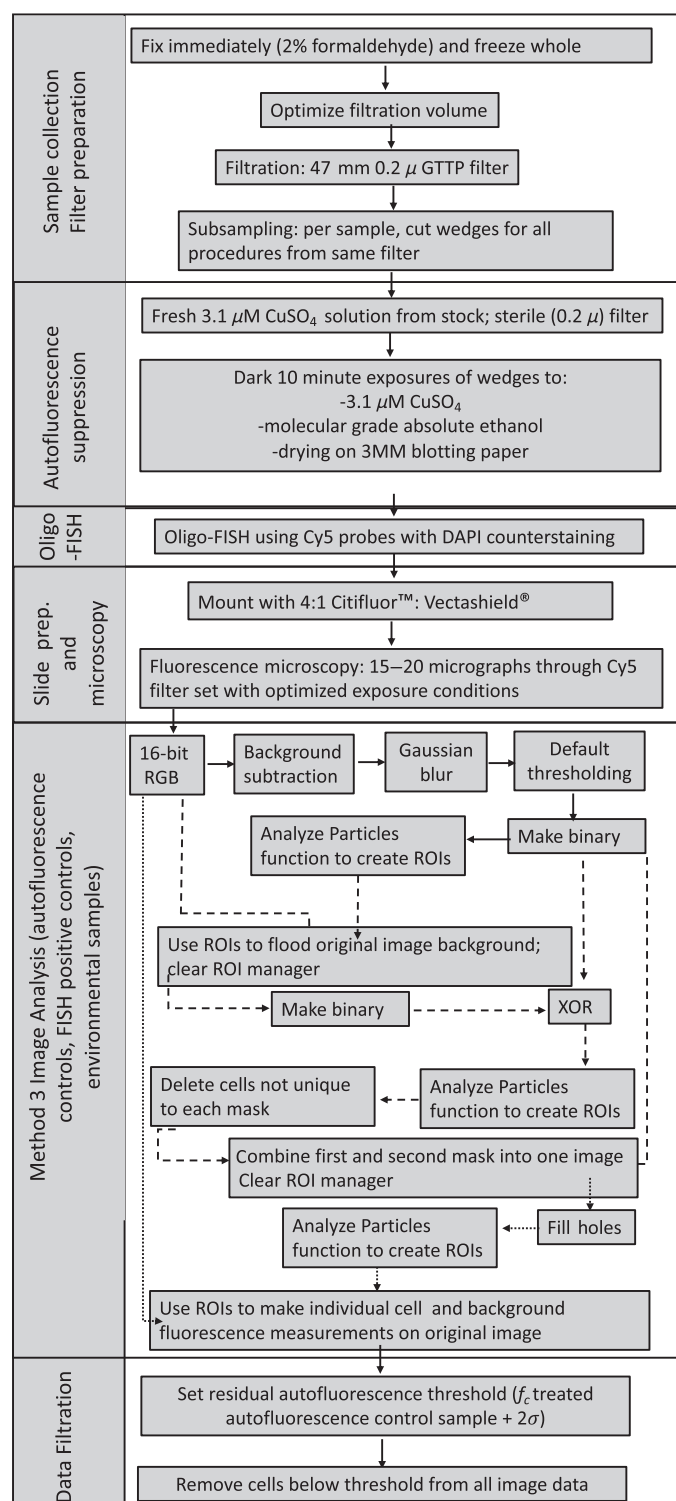
Fig 10. Recommended workflow chart for sample processing, autofluorescence suppression pretreatment, oligo-FISH, fluorescence microscopy, image analysis, and data filtration to accurately enumerate FISH targets in cyanobacteria-rich samples. All of these steps should be followed for environmental samples. The data filtration step should be excluded from autofluorescence control and pure culture (probe-positive) analyses.

then lamp intensities over the course of a set of observations may vary sufficiently to compromise background corrections. Likewise, changing the mercury lamp over the course of a set of observations will introduce the same concerns and may necessitate preparing new controls for subsequent image processing. Similarly, if the CuSO$_4$/EtOH-treated filters are intended for microspectroscopy work (example: Raman-FISH), the pretreated and control images both need to be acquired on the fluorescence microscope coupled to the instrument.

We recommend for future work that this method be evaluated in combination with multi-labeled-FISH (mil-FISH) for a greater signal to noise ratio. Mil-FISH is known to boost the intensity of the hybridized signal in samples with high autofluorescence (Schimak et al. 2015). It should be noted that micrographs of samples collected from FGL at depths corresponding to the autofluorescent cell peak are an extreme example of cell aggregation and clumping. Method 1 was successful in cases representative of most natural samples. As Python is less memory-intensive than ImageJ, efforts should be made to extend Method 1 to also quantify cell and background fluorescence.

References

Aviv, M., H. Giladi, A. B. Oppenheim, and G. Glaser. 1996. Analysis of the shut-off of ribosomal RNA promoters in *Escherichia coli* upon entering the stationary phase of growth. FEMS Microbiol. Lett. **140**: 71–76. doi:10.1111/j.1574-6968.1996.tb08317.x

Bankhead, P. 2013. Analyzing fluorescence microscopy images with ImageJ. Nikon Imaging Center, Heidelberg Univ., Queen's Univ. Belfast.

Christoffersen, K. 1996. Ecological implications of cyanobacterial toxins in aquatic food webs. Phycologia **35**: 42–50. doi:10.2216/i0031-8884-35-6S-42.1

Cline, J. D. 1969. Spectrophotometric determination of hydrogen sulfide in natural waters 1. Limnol. Oceanogr. **14**: 454–458. doi:10.4319/lo.1969.14.3.0454

Cogdell, R. J., A. M. Hawthornthwaite, M. B. Evans, L. A. Ferguson, C. Kerfeld, J. P. Thornber, F. van Mourik, and R. van Grondelle. 1990. Isolation and characterisation of an unusual antenna complex from the marine purple sulphur photosynthetic bacterium *Chromatium purpuratum* BN5500. BBA-Bioenergetics **1019**: 239–244. doi:10.1016/0005-2728(90)90199-E

Culver, D. A., and G. J. Brunskill. 1969. Fayetteville Green Lake, New York. V. Studies of Primary Production and Zooplankton in a Meromictic Marl Lake 1. Limnol. Oceanogr. **14**: 862–873. doi:10.4319/lo.1969.14.6.0862C.

Dima, A. A., J. T. Elliott, J. J. Filliben, M. Halter, A. Peskin, J. Bernal, M. Kociolek, M. C. Brady, H. C. Tang, and A. L. Plant. 2011. Comparison of segmentation algorithms for fluorescence microscopy images of cells. Cytom. Part A **79**: 545–559. doi:10.1002/cyto.a.21079

Dixon, J. M., M. Taniguchi, and J. S. Lindsey. 2005. PhotochemCAD 2. A refined program with accompanying spectral databases for photochemical calculations. Photochem. Photobiol. **81**: 212–213. doi:10.1111/j.1751-1097.2005.tb01544.x.

Du, H., R. C. A. Fuh, J. Li, L. A. Corkan, and J. S. Lindsey. 1998. PhotochemCAD: A computer-aided design and research tool in photochemistry. Photochem. Photobiol. **68**: 141–142. doi:10.1111/j.1751-1097.1998.tb02480.x.

Frankenberg, C., and J. Berry. 2018. 3.10—Solar induced chlorophyll fluorescence: Origins, relation to photosynthesis and retrieval A2, p. 143–162.*In* S. Liang [ed.], Comprehensive remote sensing. Elsevier.

Gong, W., and A. Marchetti. 2019. Estimation of 18S gene copy number in marine eukaryotic plankton using a next-generation sequencing approach. Front. Mar. Sci. **6**: 219. doi:10.3389/fmars.2019.00219

Grote, J., M. Labrenz, B. Pfeiffer, G. Jost, and K. Jürgens. 2007. Quantitative distributions of Epsilonproteobacteria and a Sulfurimonas subgroup in pelagic redoxclines of the Central Baltic Sea. Appl. Environ. Microbiol. **73**: 7155–7161. doi:10.1128/AEM.00466-07

Hallegraeff, G. M. 2010. Ocean climate change, phytoplankton community responses, and harmful algal blooms: A formidable predictive challenge. J. Phycol. **46**: 220–235. doi:10.1111/j.1529-8817.2010.00815.x

Havig, J. R., M. L. McCormick, T. L. Hamilton, and L. R. Kump. 2015. The behavior of biologically important trace elements across the oxic/euxinic transition of meromictic Fayetteville Green Lake, New York, USA. Geochim. Cosmochim. Acta **165**: 389–406. doi:10.1016/j.gca.2015.06.024

Havig, J. R., T. L. Hamilton, M. McCormick, B. McClure, T. Sowers, B. Wegter, and L. R. Kump. 2018. Water column and sediment stable carbon isotope biogeochemistry of permanently redox-stratified Fayetteville Green Lake, New York, USA. Limnol. Oceanogr. **63**: 570–587. doi:10.1002/lno.10649

Huang, W. E., A. Ferguson, A. C. Singer, K. Lawson, I. P. Thompson, R. M. Kalin, M. J. Larkin, M. J. Bailey, and A. S. Whiteley. 2009. Resolving genetic functions within microbial populations: In situ analyses using rRNA and mRNA stable isotope probing coupled with single-cell Raman-fluorescence in situ hybridization. Appl. Environ. Microbiol. **75**: 234–241. doi:10.1128/AEM.01861-08

Ibey, B. L., G. L. Cote, V. Yadavalli, V. A. Gant, K. Newmyer, and M. V. Pishko. 2003. Analysis of longer wavelength AlexaFluor dyes for use in a minimally invasive glucose sensor. In Proceedings of the 25th Annual International Conference of the IEEE Engineering in Medicine and Biology Society (IEEE Cat. No. 03CH37439). **4**: 3446–3449. doi:10.1109/IEMBS.2003.1280888.

Jezbera, J., K. Horňák, and K. Šimek. 2005. Food selection by bacterivorous protists: Insight from the analysis of the food

vacuole content by means of fluorescence in situ hybridization. FEMS Microbiol. Ecol. **52**: 351–363. doi:10.1016/j.femsec.2004.12.001

Kansole, M. M., and T. F. Lin. 2017. Impacts of hydrogen peroxide and copper sulfate on the control of Microcystis aeruginosa and MC-LR and the inhibition of MC-LR degrading *Bacterium bacillus* sp. Water **9**: 255. doi:10.3390/w9040255

Kembel, S. W., M. Wu, J. A. Eisen, and J. L. Green. 2012. Incorporating 16S gene copy number information improves estimates of microbial diversity and abundance. PLoS Comput. Biol. **8**: e1002743. doi:10.1371/journal.pcbi.1002743

Kirchman, D., J. Sigda, R. Kapuscinski, and R. Mitchell. 1982. Statistical analysis of the direct count method for enumerating bacteria. Appl. Environ. Microbiol. **44**: 376–382. doi:10.1128/AEM.44.2.376-382.1982.

Lamb, J. J., G. Røkke, and M. F. Hohmann-Marriott. 2018. Chlorophyll fluorescence emission spectroscopy of oxygenic organisms at 77 K. Photosynthetica. **56**: 105–124. doi:10.1007/s11099-018-0791-y

Lin, X., S. G. Wakeham, I. F. Putnam, Y. M. Astor, M. I. Scranton, and G. T. Taylor. 2006. Vertical distributions of prokaryotic assemblages in the anoxic Cariaco Basin and Black Sea compared using fluorescent in situ hybridization (FISH). Appl. Environ. Microbiol. **72**: 2679–2690. doi:10.1128/AEM.72.4.2679-2690.2006.

Lodish, H., B. Arnold, S. Zipursky, M. Lawrence, D. B. Paul, and J. Darnell. 2000. The three roles of RNA in protein synthesis. *In* Molecular cell biology, 4th ed. WH Freeman.

Manz, W., R. Amann, W. Ludwig, M. Wagner, and K. H. Schleifer. 1992. Phylogenetic oligodeoxynucleotide probes for the major subclasses of proteobacteria: problems and solutions. Systematic and applied microbiology. **15**: 593-600. doi:10.1016/S0723-2020(11)80121-9.

Muthukrishnan, T., A. Govender, S. Dobretsov, and R. M. Abed. 2017. Evaluating the reliability of counting bacteria using epifluorescence microscopy. J. Mar. Sci. Eng. **5**: 4. doi:10.3390/jmse5010004

Nichele, L., V. Persichetti, M. Lucidi, and G. Cincotti. 2020. Quantitative evaluation of ImageJ thresholding algorithms for microbial cell counting. OSA Continuum **3**: 1417–1427. doi:10.1364/OSAC.393971

Oelze, J. 1985. Analysis of bacteriochlorophylls, p. 257–284. *In* Methods in microbiology, v. **18**. Academic Press.

Olson, J. M. 2013. Green bacteria: The light-harvesting chlorosome, p. 513–516. *In* Encyclopedia of biological chemistry, 2nd ed. New York, NY: Plenum Press; doi:10.1007/978-1-4613-1021-1.

O'Neil, J. M., T. W. Davis, M. A. Burford, and C. J. Gobler. 2012. The rise of harmful cyanobacteria blooms: The potential roles of eutrophication and climate change. Harmful Algae **14**: 313–334. doi:10.1016/j.hal.2011.10.027

Parulekar, N. N., P. Kolekar, A. Jenkins, S. Kleiven, H. Utkilen, A. Johansen, S. Sawant, U. Kulkarni-Kale, M. Kale, and M. Sæbø. 2017. Characterization of bacterial community associated with phytoplankton bloom in a eutrophic lake in South Norway using 16S rRNA gene amplicon sequence analysis. PLoS One **12**: e0173408. doi:10.1371/journal.pone.0173408

Pedregosa, F., G. Varoquaux, A. Gramfort, V. Michel, B. Thirion, O. Grisel, M. Blondel, P. Prettenhofer, R. Weiss, V. Dubourg, and J. Vanderplas. 2011. Scikit-learn: Machine learning in python. J. Mach. Learn. Res. **12**: 2825–2830.

Permentier, H. P., S. Neerken, J. Overmann, and J. Amesz. 2001. A bacteriochlorophyll *a* antenna complex from purple bacteria absorbing at 963 nm. Biochemistry **40**: 5573–5578. doi:10.1021/bi0024308

Pernthaler, J., F. O. Glöckner, W. Schönhuber, and R. Amann. 2001. Fluorescence in situ hybridization (FISH) with rRNA-targeted oligonucleotide probes. Methods Microbiol. **30**: 207–226. doi:10.1016/S0580-9517(01)30046-6

Polli, D., G. Cerullo, G. Lanzani, S. De Silvestri, H. Hashimoto, and R. J. Cogdell. 2006. Carotenoid-bacteriochlorophyll energy transfer in LH2 complexes studied with 10-fs time resolution. Biophys. J. **90**: 2486–2497. doi:10.1529/biophysj.105.069286

Porter, K. G., and Y. S. Feig. 1980. The use of DAPI for identifying and counting aquatic microflora. Limnol. Oceanogr. **25**: 943–948. doi:10.4319/lo.1980.25.5.0943

Riccio, D., N. Brancati, M. Frucci, and D. Gragnaniello. 2018. A new unsupervised approach for segmenting and counting cells in high-throughput microscopy image sets. IEEE J. Biomed. Health Inform. **23**: 437–448. doi:10.1109/JBHI.2018.2817485

Schimak, M. P., M. Kleiner, S. Wetzel, M. Liebeke, N. Dubilier, and B. M. Fuchs. 2015. MiL-FISH: Multi-labelled oligonucleotides for fluorescence in situ hybridization improve visualization of bacterial cells. Appl. Environ. Microbiol. **82**: 62–70. doi:10.1128/AEM.02776-15

Schneider, C. A., W. S. Rasband, and K. W. Eliceiri. 2012. NIH image to ImageJ: 25 years of image analysis. Nat. Methods **9**: 671–675. doi:10.1038/nmeth.2089

Schultze-Lam, S., S. Schultze-Lam, T. J. Beveridge, and D. J. Des Marais. 1997. Whiting events: Biogenic origin due to the photosynthetic activity of cyanobacterial picoplankton. Limnol. Oceanogr. **42**: 133–141. doi:10.4319/lo.1997.42.1.0133

Sobiechowska-Sasim, M., J. Stoń-Egiert, and A. Kosakowska. 2014. Quantitative analysis of extracted phycobilin pigments in cyanobacteria—An assessment of spectrophotometric and spectrofluorometric methods. J. Appl. Phycol. **26**: 2065–2074. doi:10.1007/s10811-014-0244-3

Toropygina, O. A., Z. K. Makhneva, and A. A. Moskalenko. 2005. Reconstitution of okenone into light harvesting complexes from *Allochromatium minutissimum*. Biochemistry **70**: 1231–1237. doi:10.1007/s10541-005-0252-7.

Tromas, N., N. Fortin, L. Bedrani, Y. Terrat, P. Cardoso, D. Bird, C. W. Greer, and B. J. Shapiro. 2017. Characterising

and predicting cyanobacterial blooms in an 8-year amplicon sequencing time course. ISME J. **11**: 1746–1763. doi:10.1038/ismej.2017.58

Wells, M. L., V. L. Trainer, T. J. Smayda, B. S. Karlson, C. G. Trick, R. M. Kudela, A. Ishikawa, S. Bernard, A. Wulff, D. M. Anderson, and W. P. Cochlan. 2015. Harmful algal blooms and climate change: Learning from the past and present to forecast the future. Harmful Algae **49**: 68–93. doi:10.1016/j.hal.2015.07.009

Yakubovskaya, E., T. Zaliznyak, J. M. Martínez, and G. T. Taylor. 2019. Tear down the fluorescent curtain: A new fluorescence suppression method for Raman micro-spectroscopic analyses. Sci. Rep. **9**: 1–9. doi:10.1038/s41598-019-52321-3

Zeller, P., O. Ploux, and A. Mejean. 2016. A simple protocol for attenuating the auto-fluorescence of cyanobacteria for optimized fluorescence in situ hybridization (FISH) imaging. J. Microbiol. Methods **12**: 216–219. doi:10.1016/j.mimet.2016.01.006

Conflict of Interest

None declared.

Submitted 26 August 2020
Revised 17 February 2021
Accepted 10 May 2021

Associate editor: Christian Fritsen